

Smallest Stable Si/SiO₂ Interface that Suppresses Quantum Tunneling from Machine-Learning-Based Global Search

Ye-Fei Li^{1,*} and Zhi-Pan Liu^{1,2,†}

¹*Collaborative Innovation Center of Chemistry for Energy Material, Shanghai Key Laboratory of Molecular Catalysis and Innovative Materials, Key Laboratory of Computational Physical Science, Department of Chemistry, Fudan University, Shanghai 200433, China*

²*Shanghai Qi Zhi Institution, Shanghai 200030, China*

(Received 24 September 2021; revised 22 January 2022; accepted 25 April 2022; published 3 June 2022)

While the downscaling of size for field effect transistors is highly desirable for computation efficiency, quantum tunneling at the Si/SiO₂ interface becomes the leading concern when approaching the nanometer scale. By developing a machine-learning-based global search method, we now reveal all the likely Si/SiO₂ interface structures from thousands of candidates. Two high Miller index Si(210) and (211) interfaces, being only ~ 1 nm in periodicity, are found to possess good carrier mobility, low carrier trapping, and low interfacial energy. The results provide the basis for fabricating stepped Si surfaces for next-generation transistors.

DOI: 10.1103/PhysRevLett.128.226102

The presence of high-quality Si/SiO₂ interfaces is one of the key reasons that Si acts as the basic material of the semiconductor industry [1]. As required by ever-increasing computation power, the size of microelectronics, in particular, the dimension of field effect transistors (FETs), shrinks continuously and now reaches nanometer regimes. Consequently, the quantum tunneling due to the sharp shortening of the channel length (the distance between electrodes in FET) becomes a leading concern, which can cause severe current leakage and, thereby, high energy costs and heat generation [2]. However, the physical limit for the smallest stable Si/SiO₂ interface [3] remains largely unclear, not to mention their geometry and electronic properties. Fundamentally, this is due to the lack of predicting tools for resolving complex solid-solid interfaces.

The FET, as shown in Fig. 1, consists of a Si channel surrounded by an insulating SiO₂ and gate that connects to electrodes at two ends, referred to the drain and the source. The carrier effective mass (m^*) of the Si/SiO₂ interface is a key parameter for FETs which controls the current on and off. For the “on” state, a low effective mass is preferable that can lead to high carrier mobility ($\mu \propto 1/m^*$) [1] and, thus, large current. In contrast, the “off” state prefers the high effective mass in order to suppress the leakage current. Overall, a trade-off has to be made to achieve both low off-state current and a high on/off current ratio. Nowadays, the Si(100)/SiO₂ interface featuring the low electron effective mass is commonly selected in *n*-type devices, while the Si(110)/SiO₂ interface with the low hole effective mass is utilized in *p*-type devices [3]. To further suppress the quantum tunneling [4], one can either modify the FET architecture, e.g., from the classic planar structure to complex nanofin structure (FinFET) [5] (Fig. 1), or utilize

different interface materials, e.g., by replacing Si by MoS₂. Recently, a 1-nm-gate MoS₂ channel with m_e^* of $0.55m_e$ was reported, which shows a high on/off current ratio of $\sim 10^6$ and more than 2 orders of magnitude reduction in off-state leakage currents relative to Si (cf. $m_e^* \sim 0.19m_e$ for Si [100]) [6]. Nevertheless, Si remains the dominant semiconducting material, and how to regulate the effective mass of Si by designing optimal Si/SiO₂ interfaces is a top challenge in the field.

In the FinFET architecture, new Si/SiO₂ interfaces, particularly those with high-index facets, emerge at the fin’s sidewalls and tips. In manufacturing ever-smaller-sized FinFET, it becomes imperative to design these Si/SiO₂ interfaces to achieve high performance. The search for the optimal Si/SiO₂ interface is, however, a formidable task in theory. First, the existing simulation methods cannot predict the orientations of Si/SiO₂ interfaces. In fact, most previous calculations were carried out on low-index Si(100)/SiO₂, simply because it is the known facet in classic

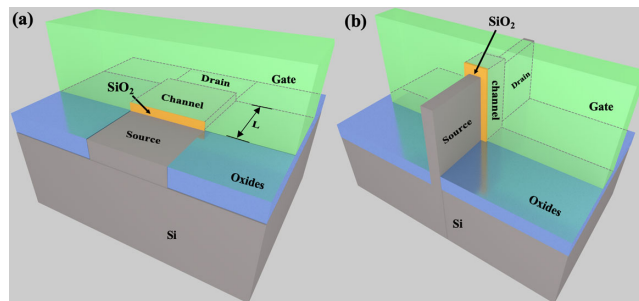


FIG. 1. Structures of FETs. (a) Classic planar FET; (b) modern FinFET. L represents the channel length.

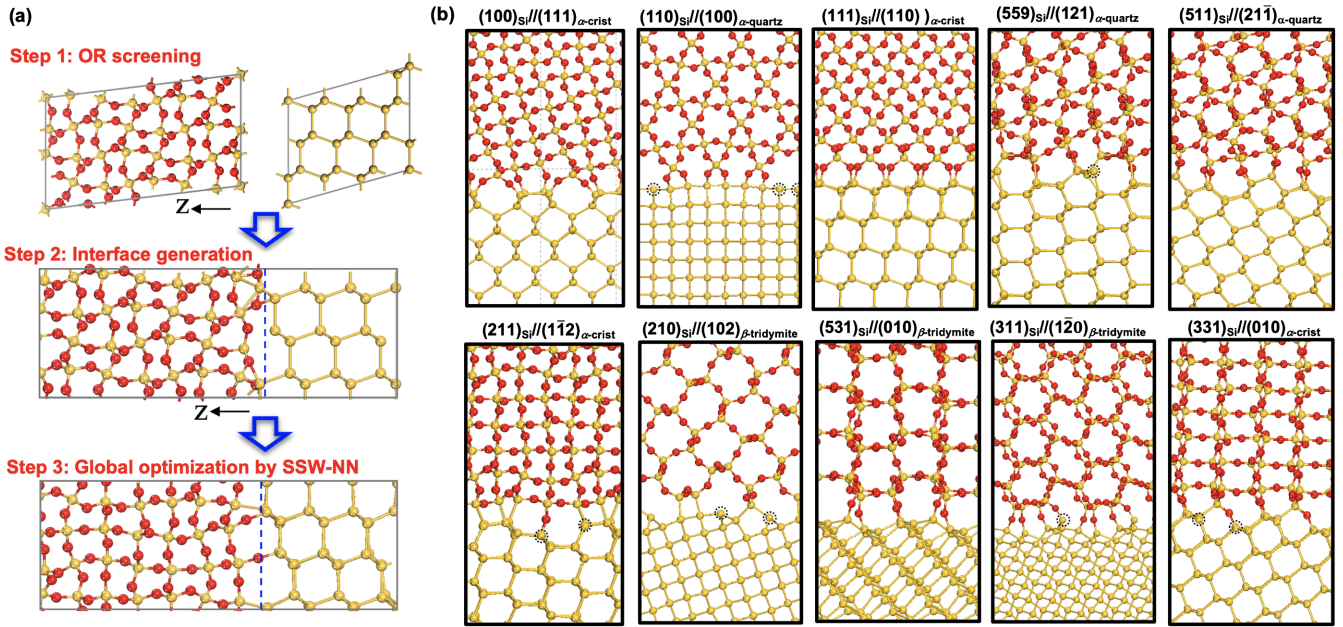


FIG. 2. (a) The flowchart of the ML-interface method. (b) Atomic structures of ten Si/SiO₂ interfaces with an interfacial area less than 1 nm² in periodicity. The dashed circles in (b) highlight the unsatisfied Si atoms with dangling bonds. Yellow balls, Si; red balls, O.

planar FETs. Second, Si facets may well undergo reconstruction due to the presence of dangling bonds, leading to the great complexity of surface structures. Third, the heterogeneous solid junction for Si/SiO₂ may well not obey the stoichiometry of chemical valence, where the Si:O may vary to reach the highest stability. In fact, bulk SiO₂ could be amorphous, which further complicates the interface formed in between Si and SiO₂, although the crystalline interface was suggested in experiments [7]. For these reasons, it remains largely unknown to date for the geometry and electronic structures of the stable Si/SiO₂ interfaces.

Herein, we develop a machine-learning-assisted phenomenological theory for the global search of interface structure between solids (ML interface). The method is utilized to predict the Si/SiO₂ interfaces by considering all the likely surface reconstructions and composition variation. Ten stable Si/SiO₂ interfaces with small interfacial area in periodicity are thus identified by density functional theory (DFT) with PBE (Perdew-Burke-Ernzerhof) exchange-correlation functional and the associated properties of the interfaces, including the interfacial-dangling-bond contents, band structure, and carrier effective mass at various Si orientations are derived from hybrid HSE06 (Heyd-Scuseria-Ernzerhof) functional.

Our ML-interface method to determine the interface structure is schematically illustrated in Fig. 2(a), which has three steps: (i) orientation relationship (OR) screening, (ii) atomic structure of interface generation from graph theory, and (iii) global optimization based on global neural network potential. Below, we briefly introduce each step, and the details are elaborated in Supplemental Material [8–10].

$$\mathbf{F} = (\mathbf{A}\mathbf{T})^{-1}\mathbf{B}\mathbf{M} = \mathbf{R}\mathbf{U}. \quad (1)$$

The first step, OR screening, aims to identify the lattice correspondence matrix \mathbf{F} between two different solid phases, as shown in Eq. (1), where \mathbf{T} and \mathbf{M} are the primitive lattice parameters of two solid phases, respectively; \mathbf{A} and \mathbf{B} are the transformation matrices that need to search. The \mathbf{F} matrix can also be decomposed into two parts: the rotation matrix \mathbf{R} and the homogeneous stretch matrix \mathbf{U} . All these matrices are (3×3) . By enumerating possible \mathbf{A} and \mathbf{B} matrices, we can obtain a series of \mathbf{U} , which can lead to the OR for the interface with the best lattice match according to the phenomenological theory of martensite crystallography (PTMC). We note that PTMC was originally developed to explain the martensitic transformation (e.g., between γ -Fe and α -Fe) by merely using the lattices of contacting phases, and it totally neglects the atomic matchness at the interface [11]. In step 2, a graph-based approach utilizes the OR obtained from step 1 to build the atomic structure of interface by gluing two surface slabs, where the max-flow min-cut algorithm from graph theory is applied to maximally retain the bonding at the interface [12]. Finally, also the most important step, our recently developed SSW-NN method; i.e., stochastic surface walking (SSW) globally optimized based on the global neural network potential [13] is utilized to extensively search for the global minimum of the interface structure built from step 2 (see Supplemental Material, Sec. 1.4 [8], for details on building the global neural network potential). As illustrated in Eq. (2), the key of the SSW method for a global PES search is the modification of PES V_{mod} by continuously adding Gaussian-type bias potential v_n along

TABLE I. The parameters for ten stable Si/SiO₂ interfaces with an interfacial area less than 1 nm².

| OR | a/a' (Å) | b/b' (Å) | θ/θ' (°) | γ (J/m ²) | m_h^* (m_e) ^a | m_e^* (m_e) ^a |
|---|-------------|-------------|----------------------|------------------------------|--------------------------------|--------------------------------|
| (100) _{Si} (111) _{α-crist} | 7.72/7.03 | 8.64/8.49 | 63/65 | 0.93 | 8.58 | 0.23 |
| (111) _{Si} (110) _{α-crist} | 6.69/6.88 | 7.72/7.03 | 90/90 | 1.13 | 0.38 | 0.94 |
| (110) _{Si} (100) _{α-quartz} | 5.46/5.46 | 15.45/14.94 | 90/90 | 1.27 | 0.32 | 16.89 |
| (531) _{Si} (010) _{β-tridymite} | 8.64/8.61 | 10.22/10.55 | 90/90 | 1.01 | 1.14 | 4.90 |
| (210) _{Si} (102) _{β-tridymite} | 5.46/5.27 | 12.21/12.56 | 90/90 | 1.16 | 0.48 | 6.76 |
| (211) _{Si} (112) _{α-crist} | 9.46/9.84 | 7.72/7.03 | 90/90 | 1.17 | 6.53 | 0.63 |
| (511) _{Si} (211) _{α-quartz} | 10.22/10.20 | 7.72/7.39 | 79/84 | 1.20 | 0.71 | 0.73 |
| (311) _{Si} (120) _{β-tridymite} | 8.64/8.61 | 8.64/9.14 | 84/90 | 1.23 | 1.07 | 3.12 |
| (559) _{Si} (121) _{α-quartz} | 7.72/7.39 | 9.46/10.20 | 90/84 | 1.27 | 0.46 | 1.05 |
| (331) _{Si} (010) _{α-crist} | 8.64/8.49 | 7.72/8.49 | 77/72 | 1.40 | 0.42 | 3.56 |

^aThe effective mass is anisotropic [14]; here, they refer to the heaviest one.

the softening mode direction N_t , which helps to overcome the barrier between minima:

$$\begin{aligned}
 V_{\text{mod}} &= V_{\text{real}} + \sum_{n=1}^{\text{NG}} v_n \\
 &= V_{\text{real}} + \sum_{n=1}^{\text{NG}} w_n \times \exp\left\{-\left[(R_t - R_t^n) \cdot N_t^n\right]^2 / (2 \times ds^2)\right\}.
 \end{aligned} \tag{2}$$

In Eq. (2), the subscript or superscript n is the index of the sequentially added bias potential, and R_t is the coordination of current structure; V_{real} is the unmodified PES; R_t^n is the coordination of reference when v_n is added. To allow the variation of atom numbers (e.g., different terminations) at the interface, the SSW-NN simulation is coupled with a grand canonical Monte Carlo (GCMC) move every 500 SSW-NN steps, where an O/Si atom can be randomly added or removed. More information on SSW and GCMC method can be found in Supplemental Material [8] and our previous work [13].

By using the above ML-interface method, we are able to search for nonstoichiometric Si/SiO₂ interface structures. Three stable SiO₂ forms, namely, α -quartz, β -tridymite, and α -cristobalite (α -crist) were considered in this Letter. We identified 2497 lattice-matched interfaces from steps 1 and 2, which has a relatively small interfacial area in periodicity that can retain high stability in a short channel. For each interface, we then carried out more than 10⁴ minima search using the SSW-NN method to find the most stable structure in step 3.

In 2497 lattice-matched interfaces, there are only 40 interfaces that have an interfacial area with periodicity less than 1 nm² [we emphasize that all possible orientations with short periodicity have been explored; see Sec. 1.1(a) of Supplemental Material [8] for more details]. By further excluding the less stable interfaces on the same Si orientation, we finally obtained ten Si/SiO₂ interfaces, as

shown in Fig. 2(b), which should, thus, represent the physical limit for the size of the Si channel. The key properties of these interfaces, including the interfacial energy and the carrier effective mass, are listed in Table I. Note that the listed data for the effective mass corresponds to the heaviest one that determines the carrier transport [14] (also see Supplemental Material [8] for more information).

Among the ten interfaces, the Si(100) interface has the lowest interfacial energy of 0.93 J/m², and the high Miller index Si(331) interface has the highest interfacial energy of 1.40 J/m². In contrary to intuition, the interfaces of some high-index Si facets, such as Si(531), can have low interfacial energy, being comparable to Si(111) and (110) interfaces that are already used in industry. It should be noticed that our ML-interface method has sampled both crystalline and amorphous structures equivalently, and it turns out that the crystalline interface is always the most stable one (see PES contour plot in Fig. S2 in Supplemental Material [8]). Our identified Si/SiO₂ interface is indeed more stable than interfacial structures proposed previously, including crystalline and amorphous ones (see Table S3 in Supplemental Material [8]), which thus supports strongly the x-ray scattering observation on the ordered SiO₂ at the interface [7].

For the carrier effective mass, the low-index Si facet Si(100) has the lowest electron effective mass ($m_e^* = 0.23m_e$), while Si(110) has the lowest hole effective mass ($m_h^* = 0.32m_e$). Both agree with the established knowledge from experiment [3]. More importantly, our results can now predict the properties of high Miller index surfaces that are still unknown from experiment: Si(331), Si(559), and (210) have low hole effective mass $\sim 0.5m_e$, while Si(211) has a low m_e^* with $0.63m_e$. They are, thus, also good candidates for FET interfaces.

Figures 3(a) and 3(b) show the dependence of the tunneling probability on the effective mass and the channel length through a 0.5-eV height potential barrier (a typical barrier height driven by gate voltage in FETs [6]).

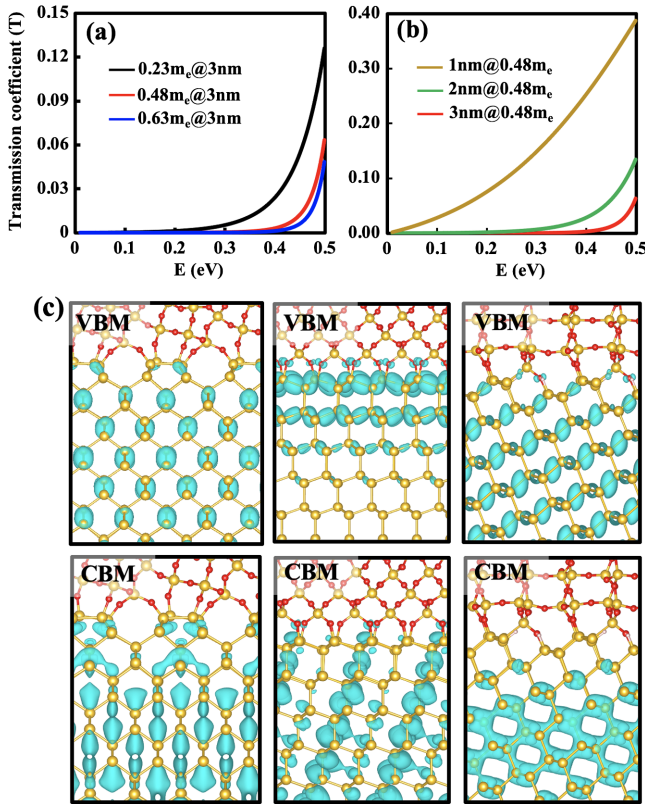


FIG. 3. (a),(b) Transmission coefficient vs incident energy for carrier tunneling through a 0.5-eV height potential barrier; (c) partial charge densities at CBM or VBM of $(100)_{\text{Si}} \parallel (111)_{\alpha\text{-crist}}$, $(111)_{\text{Si}} \parallel (110)_{\alpha\text{-crist}}$, and $(331)_{\text{Si}} \parallel (010)_{\alpha\text{-crist}}$ interfaces.

The tunneling probability is described by the transmission coefficients T in the transfer-matrix approach, which approximates an arbitrary potential profile by a stepwise one characterized by potential energy U_i in each terrace region L_i :

$$T = \frac{m_1^* k_N}{m_N^* k_1} \left(\frac{1}{M_{11}} \right)^2, \quad (3)$$

$$M = \prod_{i=1}^{i=N} \begin{bmatrix} \frac{1}{2} \left(1 + \frac{m_i^* k_{i+1}}{m_{i+1}^* k_i} \right) e^{-ik_i L_i} & \frac{1}{2} \left(1 - \frac{m_i^* k_{i+1}}{m_{i+1}^* k_i} \right) e^{-ik_i L_i} \\ \frac{1}{2} \left(1 - \frac{m_i^* k_{i+1}}{m_{i+1}^* k_i} \right) e^{ik_i L_i} & \frac{1}{2} \left(1 + \frac{m_i^* k_{i+1}}{m_{i+1}^* k_i} \right) e^{ik_i L_i} \end{bmatrix}, \quad (4)$$

where M_{11} is the element of M ; $k_i = \sqrt{2m_i^*(E - U_i)}/\hbar$ the wave vector (also see Supplemental Material [8] for more information). Figure 3(a) shows the transmission coefficients of carriers with $m^* = 0.23$, 0.48 , and $0.63m_e$ [corresponding to Si(100), (210), and (211), respectively] with a 3-nm length barrier. The results show that the increase of effective mass from 0.23 to $0.63m_e$ notably raises the onset incident energy for tunneling from 0.15 to

0.40 eV, indicating a 4-order decrease in tunneling probability according to Fermi-Dirac distribution. Note that the onset incident energy for the $0.48m_e$ carrier already reaches 0.34 eV, good enough to suppress tunneling. Figure 3(b) further displays the influence of barrier length on tunneling for $0.48m_e$ carrier, which shows that the 2-nm length barrier maintains an onset incident energy of 0.23 eV, while it diminishes at 1 nm. Therefore, we conclude that the high-index Si/SiO₂ interfaces with $m^* \sim 0.5m_e$ can efficiently suppress the tunneling down to 2 nm scale.

Below, we select $(100)_{\text{Si}} \parallel (111)_{\alpha\text{-crist}}$ and $(331)_{\text{Si}} \parallel (010)_{\alpha\text{-crist}}$ as the example to illustrate the interface atomic structure with low and high Miller index Si facets. The bare Si(100) surface exposes two-coordinated Si atoms, and, in forming the interface, these surface Si atoms pair with each other to form Si-Si dimers, leading to a (2×1) reconstruction. This turns off half of the dangling bonds, and the remaining dangling bonds are then passivated by the terminal O atoms from the SiO₂ side. It might be emphasized that our predicted (2×1) reconstruction is well consistent with the x-ray diffraction pattern of the Si(100)/SiO₂ interface in experiment [15].

For the high interfacial energy interface Si(331)/SiO₂, the exposed dangling bonds from the Si surface are not fully terminated by the SiO₂ phase. Si(331) consists of alternate (111) and (110) narrow terraces, and each Si atom on the terraces exposes one dangling bond. In forming the interface, there are still two dangling bonds per $(8.64 \text{ \AA} \times 7.72 \text{ \AA})$ unit cell untouched [highlighted by dashed cycles in Fig. 2(b)], which rationalizes the high interfacial energy of Si(331)/SiO₂.

By examining the ten interface structures [Fig. 2(b)], we find that no interfacial dangling bonds are present on the Si(100), (111), (511), and (531) faces, but Si(110), (559), (210), (211), (311), and (331) interfaces do have a number of dangling bonds. This indicates the dependence of the interfacial-dangling-bond contents on Si orientations, which can be directly measured by H₂ passivation in experiment. Indeed, Ogata *et al.* reported that the interface state densities on Si(100) and (111) have no change after H₂ passivation, indicating no dangling bonds are present on these two interfaces. In contrast, the interface state densities on Si (110), (210), (311), and (331) remarkably decrease by up to 1 order after the same treatment [16]. The experimental observations are consistent with our theoretical prediction. Since the dangling bonds are the source of interface states that trap the carrier and reduce the performance of FETs, theoretical predictions are of direct significance for the design of Si/SiO₂ interface for FETs.

Even after passivating the interfaces by H, the interface states can still persist, which can also be predicted from theory. By examining the wave functions of all ten interfaces after H passivation, as illustrated in the contour plots of conduction band minimum (CBM) and valence band maximum (VBM) (also see Fig. S3 in

Supplemental Material [8] for more information), we found that the interfaces of Si(100), (110), (210), (211), (511), (559), and (331) are ideal interfaces with no carrier trapping sites. Furthermore, Si(531) and (311) have no hole trapping site but can trap electrons at the interface due to the presence of the localized CBM. On the contrary, Si(111) has no electron trapping site but can trap holes due to the presence of localized VBM at the interface [see Fig. 3(c)].

Our data on Si/SiO₂ interfaces shed new light on the design of the next-generation FETs. To date, Si(100) and (110) are still the facets utilized in *n*-type and *p*-type devices in FinFET, respectively. However, because of their low carrier effective mass ($\sim 0.2m_e$), the off-state leakage current has limited the further decrease of the channel length. For instance, the channel length in Intel's newest 10-nm technology node is 18 nm, which is only 2 nm shorter than that in the 14-nm technology node announced in 2014. To surmount this limit, we propose that high-index Si(211) and (210) could be promising candidates for future short-channel FETs. There are several merits for these two interfaces. First, the carrier effective masses at both interfaces [$m_e^* = 0.63m_e$ for Si(211) and $m_h^* = 0.48m_e$ for Si(210)] are close to that of MoS₂ ($0.55m_e$), which can suppress the off-state leakage while maintaining the on-state current. Second, the wave functions of CBM and VBM are well delocalized within the Si phase, which restrains carrier trapping at the interface. Third, both Si(210) and (211) can form stable interfaces with SiO₂, with small interfacial energies of 1.16 and 1.17 J/m², respectively. Fourth, the size of both Si/SiO₂ interfaces is less than 1.2 nm in periodicity, which allows the downscaling of the channel length to ~ 2 nm.

To recap, we develop a ML-interface method that can systematically search for stable interfaces between any two solid phases. We now screen out ten stable Si/SiO₂ interfaces ($\gamma < 1.4$ J/m²) with an interfacial area less than 1 nm² in periodicity. Among them, Si(210) and (211) are promising candidates for the applications in the future short-channel FETs, with good carrier effective mass ($\sim 0.5m_e$), low carrier trapping, high interface stability, and short periodicity. Our results suggest that, in addition to the low-index interfaces, the high-index Si/SiO₂ interfaces do also deliver the desired thermodynamics and transport properties. With the precise control in lattice orientation, Si should still be possible to act as the key element for FinFET down to 1 nm. Our ML-interface method with only the bulk structure of material as input can be generally applied to predict the interfaces in future FETs with emerging semiconductor materials, such as SiC and GaN.

This work was supported by the National Key Research and Development Program of China (2018YFA0208600) and National Science Foundation of China (12188101, 22022301, 21773032, 21972023, 21533001, 91545107, and 91745201) and the Tencent Foundation for XPLORER PRIZE.

*yefeil@fudan.edu.cn

†zpliu@fudan.edu.cn

- [1] R. Chau, B. Doyle, S. Datta, J. Kavalieros, and K. Zhang, *Nat. Mater.* **6**, 810 (2007); A. D. Franklin, *Science* **349**, aab2750 (2015); R. Buczko, S. J. Pennycook, and S. T. Pantelides, *Phys. Rev. Lett.* **84**, 943 (2000); Y. Tu and J. Tersoff, *Phys. Rev. Lett.* **84**, 4393 (2000).
- [2] W. Cho and K. Roy, *IEEE Electron Device Lett.* **36**, 427 (2015).
- [3] W. Xiong, K. Shin, R. Cleavelin, T. Schulz, K. Schrufer, I. Cayrefourcq, M. Kennard, C. Mazure, P. Patruno, and T.-J. King Liu, *Proceedings of the 2006 64th Device Research Conference* (IEEE, PA, USA, 2006), p. 39.
- [4] V. K. Khanna, in *Integrated Nanoelectronics: Nanoscale CMOS, Post-CMOS and Allied Nanotechnologies*, edited by V. K. Khanna (Springer India, New Delhi, 2016), p. 73.
- [5] H. Xuejue *et al.*, *International Electron Devices Meeting* (IEEE, Washington, 1999), 67; A. Burenkov and J. Lorenz, *Proceedings of ESSDERC '03. 33rd Conference on European Solid-State Device Research* (2003), p. 135.
- [6] H. Barber, *Solid-State Electron.* **10**, 1039 (1967); S. B. Desai *et al.*, *Science* **354**, 99 (2016).
- [7] A. Munkholm and S. Brennan, *Phys. Rev. Lett.* **93**, 036106 (2004); A. Ourmazd, D. W. Taylor, J. A. Rentschler, and J. Bevk, *Phys. Rev. Lett.* **59**, 213 (1987); L. Forbes, W. P. Noble, and A. R. Reinberg, US patent, US6483171B1 (2002); J. Molina, C. Zuniga, W. Calleja, A. Torres, P. Rosales, E. Gutierrez, and D. L. Kendall, *Proceedings of the 2013 IEEE International Conference of Electron Devices and Solid-state Circuits* (IEEE, Hong Kong, 2013), pp. 1–2; J. Molina, J. De La Hidalga, and E. Gutierrez, *J. Appl. Phys.* **116**, 064510 (2014).
- [8] See Supplemental Material at <http://link.aps.org/supplemental/10.1103/PhysRevLett.128.226102> for details of the ML interface, which includes Refs. [9–10].
- [9] I. Krivy and B. Gruber, *Acta Crystallogr. A* **32**, 297 (1976); B. Gruber, *Acta Crystallogr. A* **29**, 433 (1973); R. W. Grosse-Kunstleve, N. K. Sauter, and P. D. Adams, *Acta Crystallogr. Sect. A* **60**, 1 (2004); L. C. Andrews, H. J. Bernstein, and N. K. Sauter, *Acta Crystallogr. Sect. A* **75**, 115 (2019).
- [10] P. Pyykkö and M. Atsumi, *Chem. Eur. J.* **15**, 186 (2009); O. Isayev, C. Oses, C. Toher, E. Gossett, S. Curtarolo, and A. Tropsha, *Nat. Commun.* **8**, 15679 (2017); V. A. Blatov, *Crystallography Reviews* **10**, 249 (2004); L. R. Ford and D. R. Fulkerson, *Can. J. Math.* **8**, 399 (1956); G. Kresse and J. Furthmüller, *Phys. Rev. B* **54**, 11169 (1996).
- [11] J. S. Bowles and J. K. Mackenzie, *Acta Metall.* **2**, 129 (1954); J. K. Mackenzie and J. S. Bowles, *Acta Metall.* **2**, 138 (1954); C. M. Wayman, *Metall. Mater. Trans. A* **25**, 1787 (1994); E. C. Bain and N. Y. Dunkirk, *Trans. AIME* **70**, 25 (1924).
- [12] M. Witman, S. Ling, P. Boyd, S. Barthel, M. Haranczyk, B. Slater, and B. Smit, *ACS Cent. Sci.* **4**, 235 (2018).
- [13] C. Shang and Z. P. Liu, *J. Chem. Theory Comput.* **9**, 1838 (2013); S.-D. Huang, C. Shang, X.-J. Zhang, and Z.-P. Liu, *Chem. Sci.* **8**, 6327 (2017); C. Shang, X. J. Zhang, and Z. P. Liu, *Phys. Chem. Chem. Phys.* **16**, 17845 (2014); X. J. Zhang, C. Shang, and Z. P. Liu, *J. Chem. Theory Comput.* **9**, 3252 (2013); S.-D. Huang, C. Shang, P.-L. Kang, and

- Z.-P. Liu, *Chem. Sci.* **9**, 8644 (2018); S.-D. Huang, C. Shang, P.-L. Kang, X.-J. Zhang, and Z.-P. Liu, *WIREs Comput. Mol. Sci.* e1415 (2019).
- [14] L. Donetti, F. Gamiz, T. Whall, D. Leadley, P.-E. Hellström, G. Malm, and M. Östling, *J. Appl. Phys.* **110**, 063711 (2011).
- [15] G. Renaud, P.H. Fuoss, A. Ourmazd, J. Bevk, B. S. Freer, and P.O. Hahn, *Appl. Phys. Lett.* **58**, 1044 (1991).
- [16] S. Ogata, S. Ohno, M. Tanaka, T. Mori, T. Horikawa, and T. Yasuda, *Appl. Phys. Lett.* **98**, 092906 (2011).